Rotational accelerations stabilize leading edge vortices on revolving fly wings

David Lentink[1],* and Michael H. Dickinson[2]

[1]Experimental Zoology Group, Wageningen University, 6709 PG Wageningen, The Netherlands and [2]Bioengineering and Biology, California Institute of Technology, Pasadena, CA 91125, USA

*Author for correspondence (e-mail: david.lentink@wur.nl)

SUMMARY

The aerodynamic performance of hovering insects is largely explained by the presence of a stably attached leading edge vortex (LEV) on top of their wings. Although LEVs have been visualized on real, physically modeled, and simulated insects, the physical mechanisms responsible for their stability are poorly understood. To gain fundamental insight into LEV stability on flapping fly wings we expressed the Navier–Stokes equations in a rotating frame of reference attached to the wing's surface. Using these equations we show that LEV dynamics on flapping wings are governed by three terms: angular, centripetal and Coriolis acceleration. Our analysis for hovering conditions shows that angular acceleration is proportional to the inverse of dimensionless stroke amplitude, whereas Coriolis and centripetal acceleration are proportional to the inverse of the Rossby number. Using a dynamically scaled robot model of a flapping fruit fly wing to systematically vary these dimensionless numbers, we determined which of the three accelerations mediate LEV stability. Our force measurements and flow visualizations indicate that the LEV is stabilized by the 'quasi-steady' centripetal and Coriolis accelerations that are present at low Rossby number and result from the propeller-like sweep of the wing. In contrast, the unsteady angular acceleration that results from the back and forth motion of a flapping wing does not appear to play a role in the stable attachment of the LEV. Angular acceleration is, however, critical for LEV integrity as we found it can mediate LEV spiral bursting, a high Reynolds number effect. Our analysis and experiments further suggest that the mechanism responsible for LEV stability is not dependent on Reynolds number, at least over the range most relevant for insect flight ($100 < Re < 14,000$). LEVs are stable and continue to augment force even when they burst. These and similar findings for propellers and wind turbines at much higher Reynolds numbers suggest that even large flying animals could potentially exploit LEV-based force augmentation during slow hovering flight, take-offs or landing. We calculated the Rossby number from single-wing aspect ratios of over 300 insects, birds, bats, autorotating seeds, and pectoral fins of fish. We found that, on average, wings and fins have a Rossby number close to that of flies ($Ro=3$). Theoretically, many of these animals should therefore be able to generate a stable LEV, a prediction that is supported by recent findings for several insects, one bat, one bird and one fish. This suggests that force augmentation through stably attached (leading edge) vortices could represent a convergent solution for the generation of high fluid forces over a quite large range in size.

Supplementary material available online at http://jeb.biologists.org/cgi/content/full/212/16/2705/DC1

Key words: leading edge vortex, stability, Coriolis, centripetal, acceleration, insect, flight, wing.

INTRODUCTION

The presence of a stable leading edge vortex (LEV) is a key feature in the unexpectedly high performance of insect wings during hovering flight (Maxworthy, 1979; Ellington et al., 1996; Dickinson et al., 1999; Srygley and Thomas, 2002). Whereas a LEV is shed after a few chord lengths of travel on a translating 2D model of an insect wing (Dickinson and Götz, 1993; Dickinson, 1994; Miller and Peskin, 2004; Lentink et al., 2008), it remains stably attached on a 3D model wing that revolves about its base (Dickinson et al., 1999; Usherwood and Ellington, 2002; Birch et al., 2004). Van Den Berg and Ellington (Van Den Berg and Ellington, 1997) note that the spiral LEV generated by their mechanical model of a hawkmoth wing is remarkably similar to the spiral LEV generated by delta and swept wings (Ellington et al., 1996; Van Den Berg and Ellington, 1997). The spiral LEVs on such swept wings are stabilized by spanwise flow induced by wing sweep, suggesting that spanwise flow is similarly critical to the stability of LEVs on insect wings (Ellington et al., 1996; Van Den Berg and Ellington, 1997). Specifically, the growth of the LEV on insect wings might be stabilized by spanwise flow in the core of the LEV, driven by the dynamic pressure gradient associated with the velocity gradient along the flapping wing, by 'centrifugal' acceleration in the boundary layer, or by the induced velocity field of the spiral vortex lines (Ellington et al., 1996). An additional hypothesis is that the flow induced by the strong tip vortices of low aspect ratio insect wings stabilizes the LEV by greatly lowering the effective angle of attack (Birch and Dickinson, 2001). An attempt to block spanwise flow using a variety of baffle found little or no effect on LEV strength or stability (Birch and Dickinson, 2001), but these experiments do not clearly identify a unique explanation for LEV stability.

In this study, we start by showing experimentally that neither the swept wing analogy nor induced flow due to the tip vortex can fully explain LEV stability on fly wings. Based on the notion that revolving insect wings also stabilize LEVs (Dickinson et al., 1999; Usherwood and Ellington, 2002; Birch et al., 2004) we then apply the Navier–Stokes equations for flapping wings using a coordinate transformation that attaches the frame of reference to the surface of the flapping wing [these equations have been derived in the accompanying paper (Lentink and Dickinson, 2009)]. This analysis shows how wing kinematics can potentially stabilize the LEV on a revolving wing. Based on the two governing dimensionless numbers, Rossby number (Ro), which measures Coriolis acceleration, and

dimensionless stroke amplitude ($A*$), which is a measure of the unsteadiness of the flow, we then carry out a set of experiments to determine whether any of these dimensionless numbers mediate LEV stability through their corresponding accelerations. Using both flow visualization and force measurements we show that Ro, and not $A*$, appears to explain LEV stability. We then compare our theoretical and experimental findings with literature on other wings and fins in nature and technology.

MATERIALS AND METHODS
The basic methods used for dynamically scaling an insect wing have been described previously (Dickson and Dickinson, 2004). We constructed a model *Drosophila melanogaster* wing from 2.0 mm thick clear acrylic plate with a (single) wingspan b_s of 0.187 m and surface area S of 0.0167 m^2. Mean chord width c is defined as S/b_s. Here and elsewhere our wing parameters (b_s, S and c) refer to single wings, not a bilateral wing pair. The force sensor connects the robot arm with the wing base, which results in a wingtip radius R of 0.254 m. The wing was attached to a force transducer in series with a 3 degree of freedom actuator which was connected to a translating robot arm immersed in a 1 m×1 m×2 m tank filled with either oil or water. The Reynolds number was calculated as: $Re=(cU_g)/\nu$, in which c is average chord length, U_g the average velocity at the radius of gyration R_g (Ellington, 1984) and ν the kinematic viscosity. The tank was filled with thick mineral oil (density ρ=840 kg m^{-3}; ν=140×10^{-6} m^2 s^{-1}) to obtain Re=110, thin mineral oil (ρ=830 kg m^{-3}; ν=11.0×10^{-6} m^2 s^{-1}) to obtain Re=1400 and water (ρ=998 kg m^{-3}; ν=1.004×10^{-6} m^2 s^{-1}) to obtain Re=14,000.

In our experiments we used the following kinematic patterns for flapping: sinusoidal motion for stroke position and smoothed trapezoidal for angle of attack motion (Dickinson et al., 1999). We based the stroke amplitude of 70° in our experiments on the free flight kinematics of six slowly hovering fruit flies (Fry et al., 2003). Insect wing kinematics has features such as advanced wing rotation, a U-shaped stroke plane and a small hump in the angle of attack motion, which we neglect here, even though some of these features are known to improve insect flight performance (e.g. Dickinson et al., 1999). Note that we use amplitude in the mathematical sense, which is equal to half the total wing amplitude as defined by Ellington (Ellington, 1984). In each flapping trial, the robot flapped for six complete periods [at averaged flapping frequencies of 0.22 Hz at Re=110, 0.23 Hz at Re=1400 and 0.20 Hz at Re=14,000]. The geometric angle of attack amplitude α_0 was varied from 0 to 90° with steps of 4.5° [for definitions of flapping kinematics see Sane and Dickinson, and Lentink and Dickinson (Sane and Dickinson, 2001; Lentink and Dickinson, 2008)]. The unidirectional revolving and translating wing kinematics consisted of a constant velocity stroke with constant acceleration and deceleration to begin and end the stroke. The duration of the acceleration was 10% of the stroke for both revolving and translating wings. As with flapping trials, α_0 was varied from 0 to 90° in steps of 4.5° The revolving wing swept over an arc of 320°; the travel distance of the translating wing was calculated such that it moved over a similar distance to the revolving wing at its radius of gyration.

We generated a range of Rossby numbers (Ro) for a particular Reynolds number (Re=1400) by elongating the robot arm by factors of 1.27 and 1.53, which increased Ro at the radius of gyration to 3.6 and 4.4, respectively. The unidirectionally and reciprocally translating wing kinematics (Ro=∞) were obtained by setting the stroke amplitude of the robot arm to zero and translating the stage to which it was fixed. The stroke amplitudes for the Ro=3.6, 4.4 and ∞ cases were calculated under the condition that the actuator

disc area (Stepniewski and Keys, 1984), swept by the wing during the stroke, was identical to within a precision of <0.1%. The average Reynolds number at R_g varies <0.5% for unidirectional and <5% for reciprocating kinematics.

Flow visualization using air bubbles
We released small air bubbles at the leading edge (~25 mm apart) and trailing edge (~30 mm apart) of the wing into the oil (at Re=110 and 1400). Air was transported to the leading and trailing edges using a 2 mm thin tube glued flush to the edge of the 2 mm thick wing such that the flow was minimally disturbed by the tube. We made holes in the tube, marked with a white dot of paint, using insect pins. The air bubbles released through these holes rise upward because they are not neutrally buoyant and thus do not form perfect streak lines. Although we were able to minimize upward velocity through minimizing bubble size by puncturing the tubing with the smallest available insect pins (for fruit flies), we could not control the bubble size accurately, resulting in differently sized bubbles with different upward speeds. Finally, we note that the bubbles initially perform trail following, yielding a higher upward velocity for bubbles in a group compared with individual bubbles. In general, however, the flow visualization matches the previously performed particle image velocimetry measurements well. This method is, therefore, particularly suited for simple 3D LEV visualization because the bubbles will be drawn into strong vortices with low pressure cores resulting in tight spirals while weaker and wider vortices will result in wider spirals of bubbles. In addition, the bubbles will be driven preferentially inward (from wingtip to base) under centrifugal loading, because of their low density. Thus, bubbles that flow outward reliably indicate outward flow.

We visualized the flow around translating and revolving wings with either unidirectional or reciprocating stroke kinematics for α_0=0, 18, 36, 45, 54, 72 and 90° For image recording we used a digital monochrome Basler camera: 656×491, sampling at 100 frames s^{-1}. For flapping wings we obtained visualizations for six flap periods. We excluded the first cycle and determined the time of bursting for the subsequent five periods at Re=1400. The moment of bursting was defined as the moment at which we first noted the appearance of a white cloudy, spiral-like, accumulation of bubbles in the vortex (which is a qualitative definition). The images have been enhanced with the Auto Contrast function of Photoshop (8.0, Adobe) and the online movies are compressed with VirtualDub (1.5.10, www.cole2k.net).

Lift and drag measurements
The lift and drag forces acting on the wing were measured with a custom-built force sensor as previously described (Dickinson et al., 1999; Birch and Dickinson, 2001; Birch et al., 2004; Dickson and Dickinson, 2004). For post-processing we down-sampled the measurements at 300 Hz, which is still approximately 1400 times the flapping frequency. The force signals were filtered offline using a zero phase delay low-pass 4-pole digital Butterworth filter. The cut-off frequency was determined such that it corresponded with an average distance traveled of 0.3 chord lengths at R_g. This distance is at least 10 times lower than the distance over which a LEV is known to shed (Dickinson, 1994; Dickinson and Götz, 1993). The forces of the wing with reciprocating kinematics (six flaps) were averaged over four cycles (2nd to 5th) whereas they were averaged between 70% and 90% of the stroke period for wings with unidirectional kinematics (to exclude the start and stop transient). The final values were obtained as an average of three trials, except for the unidirectionally translating case at Re=110 and the swept wing polars for which N=1.

For a fair comparison among experiments we calculated how effectively a wing generates force for equal dynamic pressures, which is the standard approach in engineering and animal flight literature. These force coefficients were calculated based on the mean dynamic pressure $1/2\rho\bar{V}_g^2$ which we calculated using a blade element method (Ellington, 1984; Dickinson et al., 1999; Sane and Dickinson, 2001; Dickson and Dickinson, 2004). The lift coefficient was calculated as $C_L=2\bar{L}/\rho S\bar{V}_g^2$ whereas the drag coefficient was calculated as $C_D=2\overline{DV}_g/\rho S(\bar{V}_g^2)^{3/2}$ in which V_g is the velocity at the radius of gyration, ρ the density and S the wing surface area. According to this definition, C_D reduces to the classic drag coefficient for the translational kinematics. For revolving wing kinematics, C_D is the mean drag coefficient, which is equal to the power coefficient in the case that the local drag coefficient does not change along the wing's radius.

RESULTS
Test of existing hypotheses

Using the dynamically scaled fly wing (*Drosophila melanogaster*) (Dickson et al., 1999; Dickson and Dickinson, 2004) to measure forces and visualize flows, we first tested whether wing sweep and tip effects alone could stabilize a LEV on a fly wing that was translating (but not revolving) at fixed velocity. We systematically varied sweep angle from 0 to 60° over a large range of angles of attack (0 to 90°). The results, performed at *Re* 110 and 1400, show that wing sweep cannot stabilize the LEV (Fig. 1A; supplementary material Movie 1). Further, the results at zero sweep angle indicate that the presence of a tip vortex is also insufficient to stabilize the LEV (Fig. 1B; supplementary material Movie 2). It is important to note that the exact same wing generates a stable LEV and elevated forces when revolved at constant angular velocity around its base (Fig. 1C; supplementary material Movie 3), as found by others (Dickinson et al., 1999; Usherwood and Ellington, 2002; Birch et al., 2004). The translating swept fly wing not only rapidly shed its LEV but actually generated less lift than the unswept wings at Reynolds numbers of 110 and 1400 (Fig. 2). Thus, a strict analogy of the mechanisms that operate to stabilize LEVs on swept wing aircraft does not appear to hold for insect wings. In addition, the shed LEV and low performance of an unswept, translating wing indicate that tip effects alone cannot generate a stable LEV, at least not at the aspect ratio of our model fly wing. Tip effects, however, do appear to explain LEV stability on wings with very low aspect ratios close to one and less (Winter, 1936; Ringuette, 2007).

These preliminary experiments motivated us to explicitly examine the role of revolving, propeller-like, motion in LEV stability. When hovering, most insects flap their wings back and forth in a roughly horizontal stroke plane. At each stroke reversal, the wings rapidly flip over and change direction, during which time the forces and flows are highly unsteady. The LEV created at the start of one stroke sheds, and a new counter-rotating LEV forms as the wing flips over and reverses direction (Poelma et al., 2006). However, during each half-stroke (i.e the upstroke and the downstroke), the motion is 'propeller-like' in that the wing revolves around its base at a roughly constant angle of attack (Usherwood and Ellington, 2002). Our working hypothesis was that some feature of the fluid dynamics intrinsic to this revolving, propeller-like motion is responsible for the stability of the LEV. We explored this hypothesis by first identifying a complete list of rotation-based fluid accelerations that theoretically could be responsible for LEV stability, which we then tested experimentally.
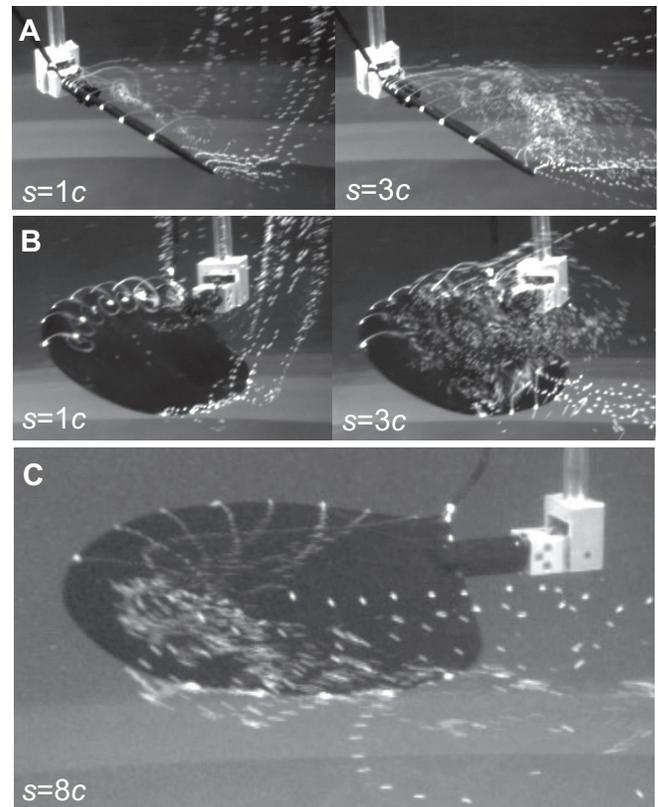

Fig. 1. The leading edge vortex (LEV) sheds from a translating model insect wing, regardless of its sweep angle, whereas it remains stably attached when the wing revolves. The LEV is visualized at Reynolds number *Re*=110 and 1400 with small air bubbles released at the leading and trailing edges of the wing. The distance (*s*) traveled by the wings is given in chord lengths *c* at the radius of gyration R_g. (A) LEVs are unstable on swept wings, shown for 40° sweep at α=36° and *Re*=1400. (B) The LEV is also unstable on the same wing without sweep. (C) Revolving the same wing results in a LEV that remains stably attached, shown for clarity at *Re*=110 and *s*=8*c*, where s is the distance traveled in chord lengths.

Navier–Stokes equations for flow near a flapping wing

We developed a simple theoretical framework to identify the dimensionless numbers that might influence flow near wings undergoing both unidirectional (propeller-like) and reciprocating (insect-like) motion during hovering conditions. A key feature of our analysis is that it accommodates a continuous range of stroke kinematics from pure revolving to pure translational motion. The analysis is continuous because translation represents the limiting case of a wing revolving over an infinitesimal angle about an infinite radius (Fig. 3A); in this sense a translating wing performs hovering flight around an infinite turning radius. For a consistent comparison among experiments, three key conditions are met with good approximation. First, the area swept by the revolving wing is kept constant, thereby maintaining constant Froude efficiency (Stepniewski and Keys, 1984). Second, the dimensionless stroke amplitude (*A**) at the radius of gyration (Ellington, 1984) is kept constant to ensure that wing–wake interactions (Birch and Dickinson, 2003) are similar. Finally, *Re* at the radius of gyration is kept constant as well (Fig. 3A). The most convenient theoretical framework for such an analysis is a dimensionless form of the Navier–Stokes equations, expressed in a non-inertial frame of reference fixed to the revolving wing in hovering flight [for
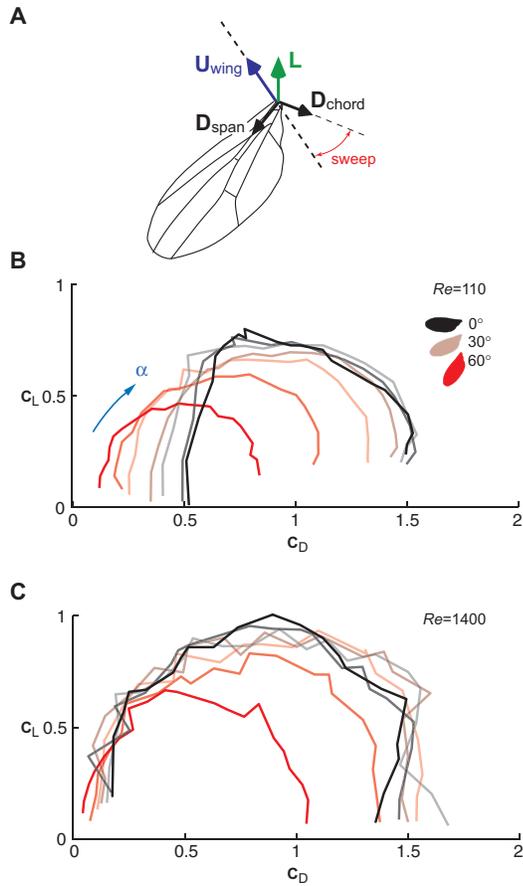
Fig. 2. Sweep does not increase the lift created by a translating fruit fly wing at Re=110 and 1400. (A) The lift (C_L)–drag (C_D) polar shown for Re=110 (B) and Re=1400 (C) represents the dimensionless lift (**L**) and chordwise drag (**D**$_{chord}$) forces obtained by varying the angle of attack (α) from 0 to 90° in steps of 4.5°. We tested this for wing sweeps from 0°, indicated with black, to 60°, indicated with red, in increments of 10° sweep.
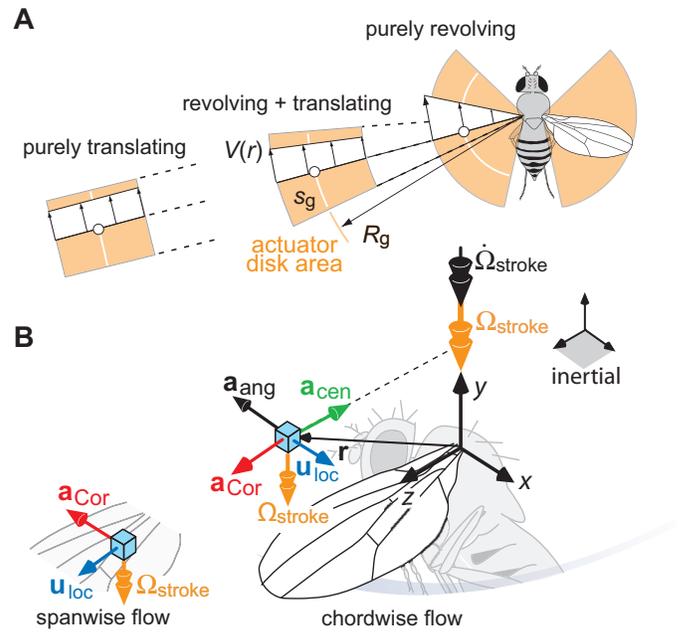

Fig. 3. (A) Framework used to analyze fluid accelerations on translating and revolving wings. The area of the actuator disc is constant within the model. R_g is the radius of gyration, s_g the number of chord lengths traveled at R_g during a full stroke, and $V(r)$ is the velocity distribution along the wing's radius r. (B) In the wing-bound frame, the fluid close to the wing experiences three accelerations due to the wing's stroke kinematics: an angular acceleration **a**$_{ang}$, a centripetal acceleration **a**$_{cen}$ and a Coriolis acceleration **a**$_{Cor}$. Note that **u**$_{loc}$ is the local velocity in the wing-bound frame, **Ω**$_{stroke}$ is the angular velocity due to stroke, **Ω̇**$_{stroke}$ is the angular acceleration due to stroke and **r** is the position of a particle of fluid in the rotating frame.

derivation see Lentink and Dickinson (Lentink and Dickinson, 2008)] (see also Vanyo, 1993; Greitzer et al., 2004). The dimensionless fluid acceleration due to net viscous and pressure forces acting on a fluid 'particle' in an inertial frame **a**$_{inert}$ is related to that in the rotating frame **a**$_{loc}$ by (Baruh, 1999):

$$\mathbf{a}_{inert} = \mathbf{a}_{loc} + (\mathbf{a}_{ang} + \mathbf{a}_{cen} + \mathbf{a}_{Cor}) , \tag{1}$$

where:

$$\mathbf{a}_{ang} = 1/A^* \cdot \dot{\mathbf{\Omega}} \times \mathbf{r} , \tag{2}$$

$$\mathbf{a}_{cen} = 1/Ro \cdot \mathbf{\Omega} \times (\mathbf{\Omega} \times \mathbf{r}) \tag{3}$$

and

$$\mathbf{a}_{Cor} = 1/Ro \cdot 2\mathbf{\Omega} \times \mathbf{u}_{loc} . \tag{4}$$

Here, **Ω** is the angular velocity and **Ω̇** is the angular acceleration of the rotating frame, and **r** and **u**$_{loc}$ are the position and velocity of a fluid volume in the rotating frame, respectively (Fig. 3B). The angular acceleration is inversely proportional to A^*, which is a measure of dimensionless stroke amplitude:

$$A^* = \Phi_0 R/c , \tag{5}$$

where Φ_0 is the stroke amplitude in radians, R is wing length, and c is the average chord length. This term expresses the amplitude as the number of chord lengths traveled.

The three terms enclosed in brackets in Eqn 1 are the angular (**a**$_{ang}$), centripetal (**a**$_{cen}$) and Coriolis (**a**$_{Cor}$) accelerations. Physically, these three accelerations result from the wing's kinematics and are enforced on the air close to the wing's surface, which can neither flow through nor slip with respect to the wing at its surface (Vanyo, 1993; Greitzer et al., 2004). We illustrate the three rotational accelerations that result from the dominant angular velocity due to stroke (Lentink and Dickinson, 2008) in Fig. 3B. The first component, **a**$_{ang}$, is the manifestation of the angular acceleration of the wing around its base, which results locally in a chordwise acceleration (Fig. 3B). This term is absent on a wing that revolves unidirectionally at constant angular speed, but will be present if the angular velocity changes, as with reciprocating back and forth motion (Fig. 3A). The second term, **a**$_{cen}$, represents the centripetal acceleration, which is directed spanwise towards the wing's base (Fig. 3B). The third term, **a**$_{Cor}$, represents the Coriolis acceleration; its direction depends on the direction of local fluid velocity **u**$_{loc}$ (Fig. 3B). Both the centripetal and Coriolis accelerations (**a**$_{cen}$ and **a**$_{Cor}$) are 'quasi-steady' in that they depend on the instantaneous value of the angular velocity **Ω** of the wing. This is in contrast to the angular acceleration (**a**$_{ang}$), which depends on changes in angular velocity **Ω̇**. Note that we consider accelerations (Eqns 2–4, Fig. 3B) instead of the analogous 'fictitious forces', which point in the opposite direction (Vanyo, 1993; Greitzer et al., 2004).

The magnitudes of the three acceleration terms $\mathbf{a}_{ang}$, $\mathbf{a}_{cen}$ and $\mathbf{a}_{Cor}$ are scaled with respect to the fluid's convective acceleration (in the local frame), which results in the three individual dimensionless numbers in Eqns 2–4. In the special case of hovering flight, both the centripetal and Coriolis accelerations are inversely proportional to the Rossby number Ro (Rossby, 1936; Lentink and Dickinson, 2008). From now on we will use the dimensionless length scales A^* and Ro to quantify the angular, centripetal and Coriolis accelerations. For a revolving wing, Ro is equal to R_g/c, the ratio of the radius of gyration divided by the mean chord length. Ro is infinite for wings that translate, because the radius of gyration is infinitely large (Fig. 3A). It is convenient to calculate the Rossby number with respect to wingtip radius, R, rather than radius of gyration:

$$Ro = R/c \,, \tag{6}$$

because this value is equivalent to the aspect ratio of a single wing AR_s and is easily extracted from the biological literature (for details, see Lentink and Dickinson, 2008). Typical values of Ro (based on wingtip radius) for insect wings cluster near 3 (Fig. 12), which immediately suggests that rotational accelerations may be significant (note $R_g/c \approx 1.5$ because $R_g \approx 0.5R$ for insects). For a reciprocating wing, A^* is equal to A/c; the ratio of stroke amplitude A to mean chord length c. Again, we consider the stroke amplitude at the wing's tip instead of the radius of gyration, for simplicity. Note that for a unidirectional revolving wing A, and therefore A^*, is infinite.

What is the relative importance of $\mathbf{a}_{ang}$, $\mathbf{a}_{cen}$ and $\mathbf{a}_{Cor}$ for insect wings? In hovering flight, the ratio of A^* to Ro (the quotient of Eqns 5 and 6) is Φ_0, where Φ_0 is the amplitude (in radians) of the harmonic function that defines the reciprocating motion of the wing (see definitions of A^* and Ro in Eqns 5 and 6). Φ_0 ranges from about 0.6 to 1.5 for insects (Ellington, 1984). Therefore A^* is of the same order of magnitude as Ro across insects, order one, which suggests that $\mathbf{a}_{ang}$, $\mathbf{a}_{cen}$ and $\mathbf{a}_{Cor}$ have similar magnitudes as well. This holds true not just for insects but also for larger animals under continuous or transient hovering conditions. Further insight can be gained by coarsely evaluating the rotational accelerations at the start, middle and end of each stroke assuming that the back and forth motion is roughly harmonic, a reasonable assumption for many insects (Ellington, 1984). At the end and start of the stroke both $\mathbf{a}_{cen}$ and $\mathbf{a}_{Cor}$ are minimal because Ω is zero, whereas $\dot{\Omega}$ and thus $\mathbf{a}_{ang}$ are maximal and scaled by $1/A^*$. However, these conditions are probably of little importance in LEV stability, because the LEV sheds and reforms (with opposite sense) during stroke reversal (e.g. see Poelma et al., 2006). At midstroke, when LEV stability is at issue, $\mathbf{a}_{cen}$ and $\mathbf{a}_{Cor}$ are maximal and scaled by $1/Ro$, whereas $\mathbf{a}_{ang}$ is near zero. This simple analysis suggests that LEV stability might be mediated by the rotational accelerations $\mathbf{a}_{cen}$ and $\mathbf{a}_{Cor}$ and not by the unsteady acceleration $\mathbf{a}_{ang}$. The primary goal of the following experimental analysis is to explicitly test this theoretical prediction.

Dependence of LEV dynamics on dimensionless numbers

We performed a series of flow visualizations and force measurements on revolving (Ro=2.9) and translating (Ro=∞) fly wings undergoing unidirectional (A^*=∞) and reciprocating (A^*=3.5) motion for angles of attack amplitudes between 0 and 90° The finite values of Ro and A^* are representative of slowly hovering fruit flies in free flight (Fry et al., 2003) and are close to the mean value found for many insects. (Note that Ro=∞ corresponds with $1/Ro$=0, i.e. Coriolis and centripetal accelerations are zero. Similarly, A^*=∞ indicates zero angular acceleration.)
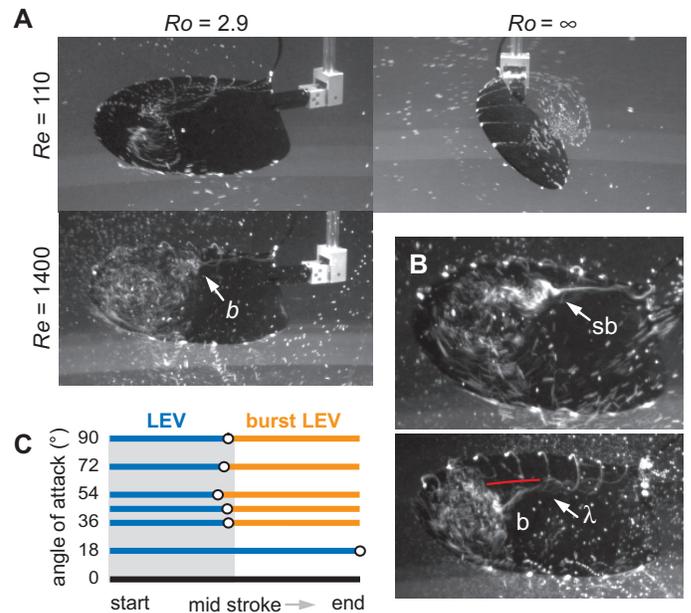

Fig. 4. Influence of Rossby number Ro on LEV stability. (A) LEV visualized on wing undergoing revolving reciprocating motion (Ro=2.9, A^*=3.5) or translational reciprocal motion (Ro=∞) at α=36°. The visualizations were made at s=4c at the radius of gyration, near the end of the stroke (4.4c). At Re=1400, the LEV bursts (b) halfway along the wing (Ro=2.9), but remains stably attached. (B) Top panel: close up of a LEV exhibiting spiral bursting (sb) at Re=1400 midway through the stroke at α=45°. Bottom panel: at the end of the stroke for α=18° at midstroke we observed that the burst LEV was λ-shaped; it split up into two 'dual vortices' near the tip, of which the bottom one, below the red line, burst spiral-like (b). (C) Observations of the occurrence of a stable LEV and the onset of spiral bursting within a stroke of a reciprocally revolving wing (Ro=2.9) at Re=1400. The LEVs are stable for all angles of attack and exhibit spiral bursting midstroke for α>18°, of which the start is indicated with a circle (diameter is larger than the s.d. calculated over five strokes).

The LEV is stable on a unidirectionally revolving wing (Ro=2.9, A^*=∞; Fig. 1C; supplementary material Movie 3), as found in prior studies (Dickinson et al., 1999; Usherwood and Ellington, 2002; Birch et al., 2004), but not on a unidirectionally translating wing (Ro=∞, A^*=∞; Fig. 1B; supplementary material Movie 2). The LEV is also stable on a reciprocally revolving wing (Ro=2.9, A^*=3.5), but not on a reciprocally translating wing (Ro=∞, A^*=3.5; Fig. 4A; supplementary material Movies 4 and 5). These results are similar at Re 110 (fruit fly scale) and 1400 (house fly or bee scale; supplementary material Movie 6). In summary, reciprocating motion (finite A^*) is not sufficient to stabilize a LEV. Rather, LEV stability appears only to require the low Ro resulting from revolving propeller-like motion.

Although we observed a stable LEV at both Re 110 and 1400 on both unidirectionally and reciprocally revolving wings, the flow structure was not identical for these Re numbers, as found previously (Birch et al., 2004). In particular, the LEVs generated in experiments at Re 1400 exhibited spiral bursting under both unidirectional and reciprocating motion (Fig. 4B; supplementary material Movie 7). The 'bursting' of a spiral vortex is a phenomenon that is thought to be initiated by deceleration of the core flow (Greenwell, 2002) and has been described for delta wings operating above a Re of about 1000. For a unidirectional revolving wing, the LEV bursts immediately after startup at angles of attack above 18°, whereas for the reciprocating case the LEV
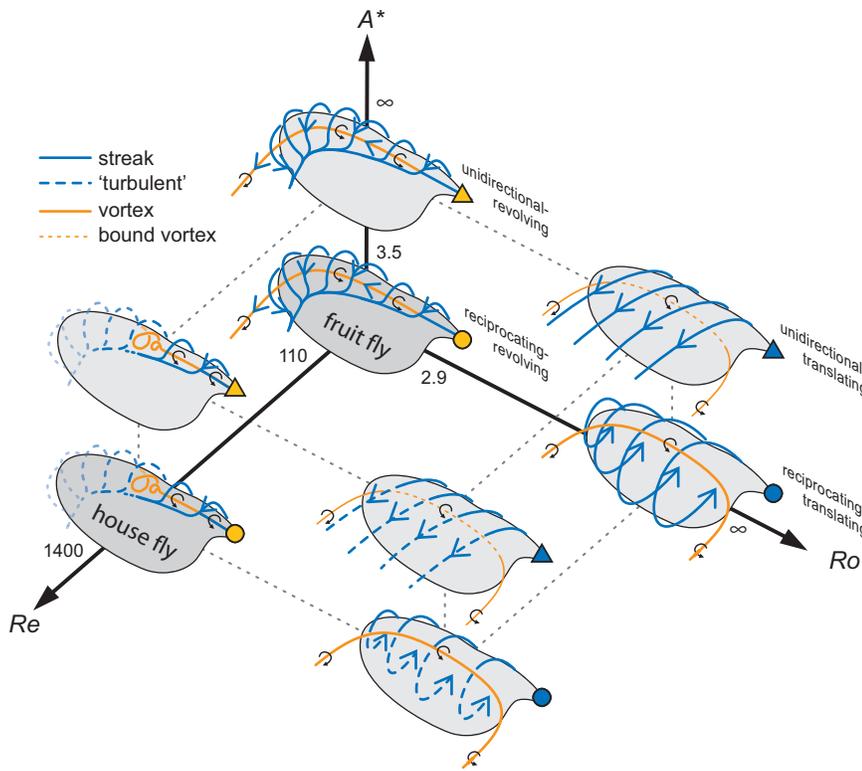
Fig. 5. Flow cartoons that summarize our flow visualization experiments as a function of Re, Ro and A^*. Low Ro (2.9) results in stable LEVs, A^* (3.5, ∞) does not modify this and higher Re (110 to 1400) induces vortex bursting, but does not affect the stable attachment of the LEV with respect to the wing. Re=110 represents fruit flies and Re=1400 house flies. Triangles represent unidirectional stroke kinematics, circles represent reciprocating stroke kinematics. Ro is indicated by color: yellow, Ro=2.9; blue, Ro=∞, as used in Fig. 6.

bursts after the wing almost reaches the midstroke position when the wing starts to decelerate (Fig. 4C). On our model insect wing, the LEV remained coherent after it burst, resulting in a 'turbulent' volume of rotating fluid whose position remained stable with respect to the wing. Examples of spiral bursting are shown in Fig. 4A for the end of a stroke at an angle of attack α=36° at midstroke and in Fig. 4B for midstroke at α=45° [note α=90°–α₀ for flapping wings (Sane and Dickinson, 2001)]. Similar to Lu

et al. (Lu et al., 2006), we observed in a few cases a double LEV structure with a small LEV in front of a larger burst LEV (Fig. 4B).

We summarize our basic flow visualizations in Fig. 5 using cartoons to indicate the basic flow structure at different values of A^*, Ro and Re. It shows that revolving wings (Ro=2.9) mediate compact and stable spiral LEVs, whereas the LEV is unstable for translating wings (Ro=∞). Reciprocating motion (A^*) does not modify LEV stability, but at small stroke amplitudes it does,
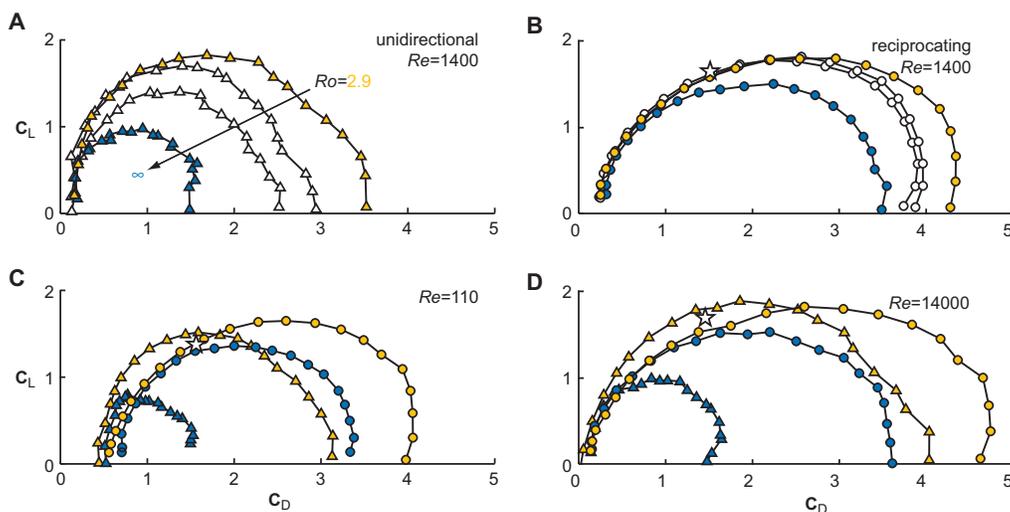

Fig. 6. The lift and drag coefficients of revolving wings (low Ro) are larger than those generated by translating wings (high Ro) at Re=110, 1400 and 14,000. The lift (C_L)–drag (C_D) polars shown are obtained by varying the angle of attack from 0 to 90°. in steps of 4.5°. Triangles represent unidirectional stroke kinematics, circles represent reciprocating stroke kinematics. Ro is indicated by color: yellow, Ro=2.9; blue, Ro=∞; white, Ro=3.6 and Ro=4.4. (A,B) At Re=1400, the lift and drag coefficients depend directly on Ro for both unidirectional and reciprocating stroke kinematics. The force augmentation of the unstable LEV on the translating reciprocating wing in B is still substantial compared with the performance of a unidirectional translating wing (A). (C,D) Force augmentation at low Ro is found from Re=110 to 14,000.
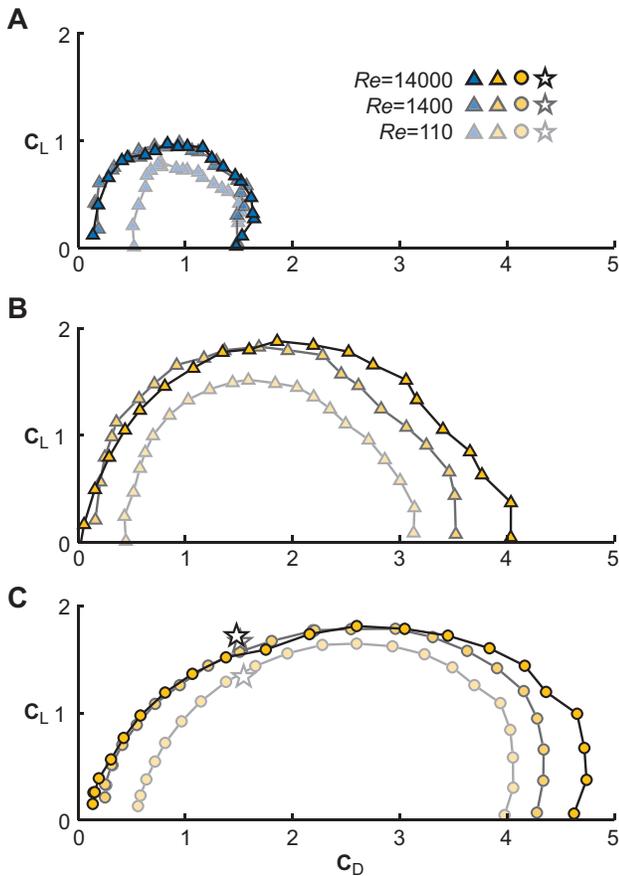
Fig. 7. Lift and drag augmentation of the LEV varies little with Reynolds number. (A) Unidirectionally translating wing. (B) Unidirectionally revolving wing. (C) Reciprocally revolving wing; star represents fruit fly kinematics. The force polars at *Re* 1400 and 14,000 overlap for angles of attack lower than 45°. The main effect of a low Reynolds number (110) is that it damps both lift and drag force.

however, keep the LEV close to the wing as it sheds the unstable LEV in time and forms a new one (with opposite sense) during every stroke reversal (*A**=3.5). For higher stroke amplitudes this does not work because the LEV sheds before stroke reversal; unidirectional translational motion being the limiting case (*A**=∞). Reynolds number does not seem to affect LEV stability within the range examined. An increasing Reynolds number does, however, modify LEV integrity as it induces vortex bursting on revolving wings. On translating wings we did not observe vortex bursting but the flow did become more erratic after a tight vortex was formed and started to separate from the wing, suggesting a transition to turbulent flow.
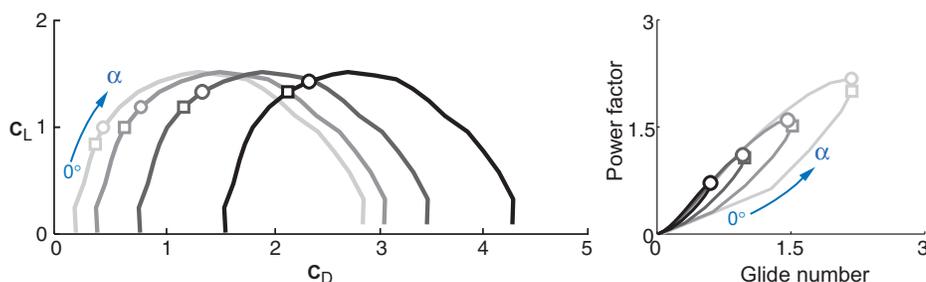
Dependence of force coefficients on dimensionless numbers

One critical question in assessing the efficacy of LEVs at different *Re* is whether a burst LEV still augments the force generated by the wing. To address this, we measured the forces generated by the model fly wing under different kinematic conditions. Comparing the lift and drag coefficients (C_D and C_L) generated at *Re*=110 and 1400 under the four kinematic conditions discussed above (the four combinations of *Ro* and *A** in Fig. 5) indicates that bursting does not result in a loss of force augmentation (Fig. 6A–C; Fig. 7). On the contrary, force coefficients are actually elevated at higher *Re*, as has previously been reported (Birch et al., 2004). The presence of a stably attached LEV at low *Ro* (revolving motion) was in all cases accompanied by an increase of the lift and drag coefficients relative to the *Ro*=∞ case (translational motion).

To test whether LEV stability and force augmentation depend directly on *Ro*, we varied *Ro* for both a unidirectionally and a reciprocally revolving wing. This was achieved experimentally by extending the wing away from its rotational axis to create *Ro* values of 3.6 and 4.4 (*Re*=1400). Force augmentation decreased with increasing *Ro* (Fig. 6A,B), consistent with the general prediction that the LEV is stabilized at low *Ro*. However, we saw no evidence for LEV shedding in our force or video records under these conditions. We speculate that within the permissive range of low *Ro* the precise magnitude of rotational accelerations may influence equilibrium conditions and determine the strength and efficacy of the LEV.

The observation that the LEV was stable even after it had burst encouraged us to test whether LEV force augmentation might extend to even higher *Re*. At *Re* 14,000 (hummingbird scale) we continued to find force augmentation (Fig. 6D). In Fig. 7 it can be seen that aerodynamic force polars of flapping, spinning and translating wings depend only weakly on *Re*. Important *Re* effects do, however, still exist as the minimum drag coefficient at zero lift, C_{D0}, decreases with increasing Reynolds number.

Efficacy of flapping, spinning and translating fly wings

In the past, performance analyses of insect wings have been focused primarily on maximum lift production, which is augmented by the LEV, but how efficient is this high-lift mechanism? To assess aerodynamic efficacy, we constructed 'performance polars' using two relevant indices: glide number, C_L/C_D, and power factor, $C_L^{3/2}/C_D$ (e.g. Ruijgrok, 1994; Wang, 2008). The required power for a certain amount of lift decreases with increasing power factor. Fig. 8 shows how force and performance polars are related. We further illustrate the effect of decreasing C_{D0}, which increases performance; the corresponding performance maxima occur at lower angles of attack for lower C_{D0}. The power factor is maximal (Fig. 8, circle) at an angle of attack that is slightly higher than the one for which the glide number is maximal (Fig. 8, square) (Ruijgrok, 1994).

Insects use reciprocally revolving wings to generate lift, whereas helicopters use spinning blades and airplanes simply translate their

Fig. 8. Illustration of how the lift–drag polar is related to the performance polar. Decreasing minimum drag coefficient, which occurs for increasing Reynolds number, increases performance (starting with black and ending with gray we plot polars for drag coefficient at zero lift C_{D0}=1.6, 0.8, 0.4, 0.2, 0.1). A circle indicates maximum power factor and a square maximum glide number.
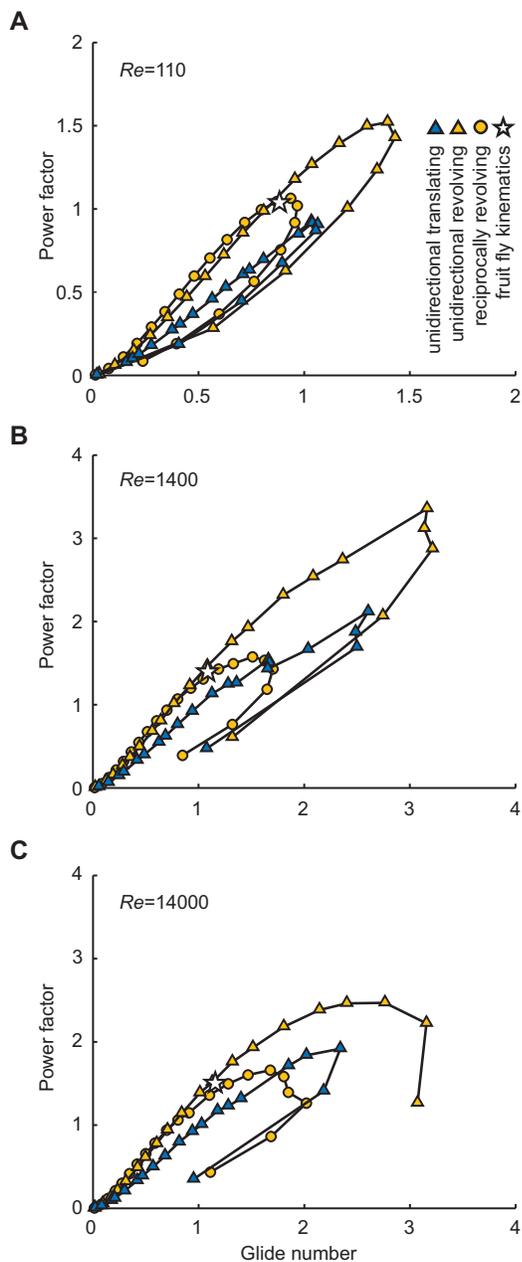
Fig. 9. Spinning fly wings outperform translating and flapping fly wings at 110<*Re*<14,000 (A–C). The same symbols are used as in Figs 6 and 7. Maximal power factor represents the minimum aerodynamic power required to hover. Fruit fly kinematics is indicated with a star; note that this corresponds approximately to minimal power required to hover (maximal power factor) at *Re*=110, at which they operate. At higher *Re*, fruit fly kinematics also do well for hovering at minimal power, although the power factor is slightly below optimal (B,C).

wings through air. Based on Fig. 7 we can readily infer that flapping and spinning fly wings generate easily up to twice as much lift and drag force compared with translating fly wings for 110<*Re*<14,000. But which kinematics generates lift most efficiently? For *Re*=110–14,000 we find that the spinning fly wings perform up to 100% better than flapping fly wings and up to 50% better than translating fly wings, as measured by power factor (Fig. 9). Further, for 1400<*Re*<14,000 we find that translating wings also outperform flapping wings, whereas flapping fly wings slightly outperform

translating wings at *Re*=110 (fruit fly scale). Our measurements show that fruit flies actually flap their wings with kinematics that are near optimal with respect to power factor; their wing kinematics results in a hovering performance that matches well the peak performance for our simplified robot kinematics at *Re*=110 (Fig. 9). As Reynolds number increases, the angle of attack corresponding with minimum power decreases, indicating that less prominent LEVs result in maximal hover efficiency. This analysis, however, assumes that power factor is the most appropriate measure of general performance. If maximum lift were limiting, one would reach quite different conclusions as maximum lift occurs at roughly α=45°, quite independent of *Re*.

DISCUSSION

Using a dynamically scaled robot fly wing we visualized the flow and measured the corresponding lift and drag forces that result from a range of wing kinematics at 110<*Re*<1400. We tested swept wings and revolving and translating wings undergoing unidirectional and reciprocating motion. This allowed us to determine which kinematics results in stable LEVs, maximum lift augmentation and maximum aerodynamic performance. Ultimately this test allowed us to determine which dimensionless number and corresponding rotational accelerations best predict LEV stability.

Rossby numbers of order one mediate stabile LEVs

Our results suggest that the centripetal $\mathbf{a}_{cen}$ and Coriolis $\mathbf{a}_{Cor}$ accelerations mediate the stability of a LEV on a unidirectional and reciprocally revolving insect wing (Fig. 5), and that these rotational accelerations are inversely proportional to Rossby number (*Ro*). The decrease in force augmentation from *Ro*=2.9 to 3.6 to 4.4 (Fig. 6A,B) suggests that LEV stability is confined to *Ro* of order one or lower. However, high aspect ratio revolving wings still experience significant rotational accelerations near the root were the radial position *r* is small compared with chord length *c* and thus could locally support a stable LEV. This effect is likely responsible for the higher than expected forces found near the hub of high aspect ratio wind turbine blades where local *Ro*=*r*/*c* is less than 3 (Tangler, 2004), a phenomenon that has been confirmed by computational fluid dynamic (CFD) simulations (Beom-Seok et al., 2002). Locally at *r*/*c*<3 the Coriolis and centripetal accelerations are high as the local values are inversely proportional to the local Rossby number *r*/*c*, irrespective of the Rossby number that represents the whole wing (*R*/*c*), which is high for high aspect ratio wings. The LEV visualizations of Lu et al. (Lu et al., 2006) on flapping high aspect ratio wings (*Ro*=1.3–10) suggest that the most prominent LEV (they found dual vortices for *Re*>640) is indeed confined to the base region where local *Ro* is approximately lower than 3. This confirms the idea that a slender wing can locally support a stable LEV near the base where the local Rossby number *r*/*c*<3, which yields locally significant rotational flow accelerations.

Our theoretical prediction and experimental confirmation suggest that rotational accelerations mediate LEV stability, but how are $\mathbf{a}_{cen}$ and $\mathbf{a}_{Cor}$ physically involved? On wind turbines, operating at *Re* of order 10^6, $\mathbf{a}_{cen}$ has been attributed to centrifugal pumping (e.g. Lindenburg, 2004; Vanyo, 1993; Greitzer et al., 2004), which results in an outward spanwise flow near the hub. At the hub the blade undergoes so-called '3D stall' and generates elevated lift forces resulting in local lift coefficients well above 2 (Tangler, 2004). The flow pattern in the hub region of a wind turbine, where local *Ro* is similar to that of insect wings, is distinct from the pattern more distally, where the slender blades are said to undergo '2D stall' (Beom-Seok et al., 2002; Tangler, 2004; Lindenburg, 2004).
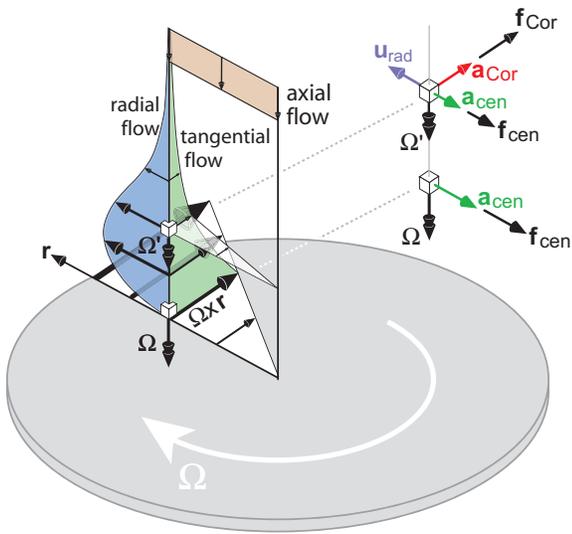
Fig. 10. Boundary layer on a spinning disc [after Vanyo (Vanyo, 1993)]. A rotating boundary layer is commonly referred to as the Ekman layer and the axial flow towards the wing, needed to balance the radial flow, is referred to as Ekman pumping. The boundary layer velocity profile is self-similar in that it scales with angular velocity multiplied by radial distance. Therefore, the velocity profiles shown depict the whole velocity field. The pressure field is rotationally symmetric and does not vary with radius; it only varies with the axial distance from the disc. The forces needed to support Coriolis and centrifugal accelerations are therefore solely due to friction, which is proportional to the velocity gradient. Whereas solving the Navier–Stokes equations on revolving wings is practically impossible in the inertial (lab) reference frame, because of the surface tracking needed, in the special case of spinning discs it is easiest to solve the equations in the inertial (lab) frame. The reason for this is that the disc surface fills an infinite plane and does not need to be tracked, which simplifies the mathematics dramatically. Note that $\mathbf{\Omega}$ is the angular velocity of the disc and the fluid particle that sticks to it, $\mathbf{\Omega'} < \mathbf{\Omega}$; $\mathbf{r}$, radial vector; $\mathbf{u}_{rad}$, radial velocity; $\mathbf{a}_{cen}$, centripetal acceleration; $\mathbf{a}_{Cor}$, Coriolis acceleration; $\mathbf{f}_{Cor}$, normalized coriolis force; $\mathbf{f}_{cen}$, normalized centripetal force.

For simple rotating discs, the outward radial fluid flow mediated by centripetal acceleration of the disc is well known (e.g. Vanyo, 1993). The radial flow is limited to a boundary region known as the Ekman layer (Fig. 10). The corresponding Ekman number, $Ek=\nu/\mathbf{\Omega}c^2$, is a measure of the ratio of viscous forces to Coriolis accelerations in this boundary layer. In the case of revolving discs and wings, Ek is equal to Ro/Re; hence, one can independently choose any pairwise combination of Ek, Ro and Re as the set of characteristic dimensionless numbers (Vanyo, 1993; Greitzer et al., 2004). The first set, Re and Ro, is preferable for analyses of biological flight, because Re is more widely reported in the literature. In the Ekman layer, the fluid at the surface of the spinning disc has the same angular velocity as the disc (due to the no-slip condition at the surface) and therefore undergoes a centripetal acceleration $\mathbf{a}_{cen}$ equal to that of the spinning disc, supported by a radial friction force $\mathbf{f}_{cen}$. A bit higher above the surface of the disc, the fluid is pulled along in a tangential direction because of friction, but at the same time it slips outward radially. It slips because there is not a large enough friction force (from the gradient of radial velocity) to support the full centripetal acceleration acquired by the fluid at the disc's surface. While slipping radially outward the fluid particle undergoes Coriolis acceleration $\mathbf{a}_{Cor}$ in a tangential direction, because it speeds up to match the higher tangential velocity outward and changes direction (it rotates while pulled along by the disc).

This Coriolis acceleration is supported by a tangential friction force $\mathbf{f}_{Cor}$ that results from the tangential flow gradient in an axial direction. Even higher above the disc's surface the boundary layer ceases to exist. Because mass is conserved, the outward radial flow of fluid must be supplied with 'fresh' fluid that flows towards the disc in an axial direction. This process is called Ekman pumping.

The region of outward radial flow on top of a spinning disc is also a conspicuous feature found on top of insect wings (Maxworthy, 1979; Ellington et al., 1996; Birch and Dickinson, 2001; Birch et al., 2004; Poelma et al., 2006) and near the hub of both propellers (Himmelskamp, 1947) and wind turbines (Tangler, 2004; Lindenburg, 2004) where Ro is low locally. In fact, Ekman-like boundary layer profiles have been calculated for wind turbine blades (Dumitrescu and Cardos, 2003). Important historic evidence for spanwise flow on a propeller at low Ro can be found in Himmelskamp (Himmelskamp, 1947), a classic reference in wind turbine literature. In Fig. 11, we reproduce his visualizations of spanwise flow on a low aspect ratio propeller. Early spanwise flow visualizations and measurements on insect wings suggested that spanwise flow is confined primarily to the fluid region occupied by the core of the LEV (Maxworthy, 1979; Ellington et al., 1996). Later digital particle image velocimetry (DPIV) measurements of unidirectional and reciprocating revolving model fruit fly wings have show that spanwise flow is not primarily confined to the LEV, but extends all the way to the trailing edge (Birch and Dickinson, 2001; Birch et al., 2004; Poelma et al., 2006). Concurrently to the spanwise flow there is significant flow in an orthogonal direction, parallel to the axis of rotation, which suggests Ekman-like pumping. This flow is even visible quite far from the wing's surface (Birch et al., 2004; Poelma et al., 2006). The region of radial flow and the orthogonal flow towards the 'hub' of the wing on inclined reciprocating and unidirectional revolving insect wings indicate the presence of an Ekman-like boundary layer, although because of 'flow separation' its spatial extent is much larger (Fig. 12A) (Vanyo, 1993).

Our measurements and the observations for spinning discs, wind turbines and a propeller suggest that the spanwise flow results from 'centrifugal pumping' as the fluid near the wing's surface slips radially outward. The fluid slips because there is not enough friction to support the full centrifugal acceleration $\mathbf{a}_{cen}$ that the fluid requires at the wing's surface (Fig. 12A,B). In these cases, the centripetal acceleration also results from a net specific force directed towards the wing base ($\mathbf{f}_{cen}$ in Fig. 12B) that is presumably composed of both a pressure component and the friction component that would be present on a spinning disc (Fig. 10). All these findings strongly suggests that centrifugal pumping due to wing rotation at low Ro can be found for both low and high Re – from insect wings to wind turbine blades.

The observation that the region of separated spanwise flow (which includes the LEV, Fig. 5) stays stably attached to a revolving wing implies that it is subject not only to a centripetal acceleration $\mathbf{a}_{cen}$ but also to a continuous acceleration in the chordwise direction. The required acceleration for this kinematic condition is precisely the Coriolis term $\mathbf{a}_{Cor}$ (similar to the flow on spinning discs). This implies that the spanwise flow driven by $\mathbf{a}_{cen}$ is stabilized with respect to the wing through $\mathbf{a}_{Cor}$, which must be supplied by a net specific chordwise force that points in the direction of travel ($\mathbf{f}_{Cor}$ in Fig. 12B). Lindenburg (Lindenburg, 2004) showed that if $\mathbf{a}_{Cor}$ is supported by a fore–aft pressure gradient acting across the region of spanwise flow it could account for the elevated forces generated close to the hub of a wind turbine. Whether this force augmentation model works quantitatively for flapping insect wings is unknown, but could be examined in future research.
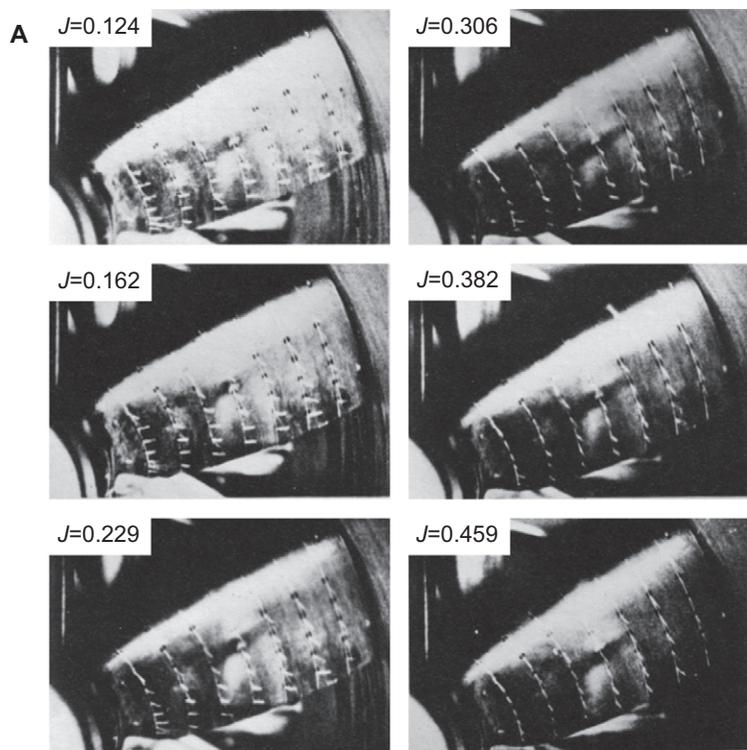
Fig. 11. Elevated forces and spanwise flow on a stubby operating propeller at $Ro<2$ and $Re=280{,}000$. (A) These unique tuft-based flow visualizations made by Himmelskamp (Himmelskamp, 1947) have never been published in a journal and are therefore reproduced here. The advance ratio J of the propeller is calculated as the ratio of forward speed and wing tip speed; it varies from 0.124, almost hovering conditions, to 0.459, forward flight conditions. The tufts indicate increasingly strong spanwise flow at low advance ratios approaching hover conditions. This spanwise flow corresponds with elevated lift. (B) For completeness we have also reproduced a sketch of the propeller and the measured section lift coefficients, based on pressure measurements at radial stations, published by Schlichting (Schlichting, 1979). Note that R is the wing tip radius, r the local radius, α the angle of attack and C_a the section lift coefficient. The maximum section lift coefficient of 3 is well above the maximum lift coefficient generated by the same airfoil in a wind tunnel (dashed line). Inboard sections, where Ro is lowest, correspond with maximum lift, which is also due to the twist in the propeller blade.
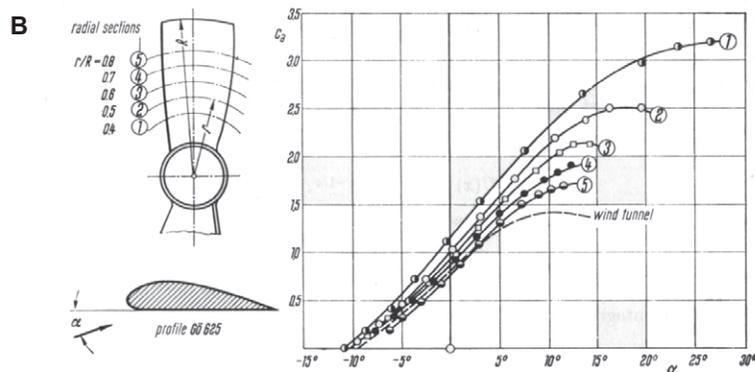
Our qualitative analysis of centripetal and Coriolis acceleration holds globally for the whole region of spanwise flow, but perhaps not in detail. For calculating the detailed acceleration distribution, and corresponding local directions, the velocity field is needed. Sun and Wu (Sun and Wu, 2004) calculated this velocity field around a unidirectional revolving insect wing at $Re=480$ using CFD. Based on the velocity field they computed the 'fictitious forces', which point in the opposite direction to the corresponding rotational accelerations (Vanyo, 1993; Greitzer et al., 2004). Their computation of the spanwise components of the 'Coriolis force' and 'centrifugal force' in the boundary layer flow for an angle of attack of 40° confirms that Coriolis and centrifugal accelerations are indeed significant. They further found that the radial pressure gradient force, due to the linear spanwise velocity distribution, is even larger and concentrated in the LEV, which can therefore explain spanwise flow in the whole LEV at $Re=480$. But the pressure gradient force is also significant in other regions where there is no spanwise flow. In the light of this, we note that the DPIV measurements of Birch et al. (Birch et al., 2004) at $Re=110$ and 1400 show significant chordwise velocity in extended regions below, in front of, and above a fly wing, without spanwise flow. This is significant, because in this region viscous effects from the wing's surface are negligible, so the viscous 'centrifugal pumping' mechanism cannot work. The pressure gradient force in this region is, however, non-zero because chordwise flow varies radially from wing root to tip, which again should drive a spanwise flow if such gradients were effective, but this does not seem to be the case. Thus, there appears to be no one-to-one link between spanwise flow and pressure gradient force throughout the flow field around a fly wing at both low and high Re. Most likely spanwise flow due to a pressure gradient is primarily confined to the core of the LEV. Aono and co-workers (Aono et al., 2008) further show that little spanwise flow and pressure gradient exists in the LEV of a fruit fly at $Re=134$, while they do find significant spanwise flow behind the LEV. For a hawkmoth at $Re=6300$ they did find strong spanwise flow and pressure gradient in the LEV. These findings of spanwise flow agree with our findings as well as those of Birch et al. (Birch et al., 2004). Aono and co-workers further suggest that Coriolis and centripetal accelerations are the likely candidates for explaining the spanwise flow they found behind the LEV on fruit fly wings.

Integrating all these observations, including our theoretical predictions and experimental confirmation, we conclude that: (1) the spanwise flow in the core of the LEV of an insect, when present, is most likely to be driven by the spanwise pressure gradient; (2) the spanwise flow in the extended viscous flow region behind the LEV can be explained best by centrifugal pumping, directly analogous to that found on spinning discs, propeller blades and wind turbine blades.

LEV integrity is mediated by *Re* and *A**

Similar to findings of vortex breakdown by van den Berg and Ellington (van den Berg and Ellington, 1997) and Lu et al. (Lu et al., 2006) we found that the LEV on a fly wing exhibits spiral bursting at *Re* 1400. Spiral bursting is a phenomenon that has been described for delta wings operating above a critical *Re* of about 1000, and is thought to be initiated by core flow deceleration (Greenwell, 2002). If we assume that the flow around an insect wing, including the core of the LEV, accelerates when the wing accelerates, we can qualitatively understand why the LEV starts to burst near midstroke when the wing, and therefore the LEV's core, starts to decelerate. This shows that, although *A** does not affect LEV stability, the corresponding angular acceleration can mediate LEV integrity. Vortex bursting may explain the erratic velocity vectors in the LEV found during previous quantitative flow measurements under similar conditions (Birch et al., 2004). Finally, our measurements show that the force coefficients do not decrease as a result of vortex bursting (Figs 5 and 6). This suggests that LEV-based force augmentation is robust to high *Re* number effects.

Comparing old and new LEV stability hypotheses

How do our findings relate to the previous ones that resulted in the swept wing analogy and tip vortex hypothesis? We found that LEV stability induced by the tip vortex does not seem to work for fly wings at *Re*=110 and 1400 (Figs 1 and 2), although there is evidence for higher Reynolds numbers that translating stubbier wings with an aspect ratio of roughly one (and less) does generate stable LEVs (Winter, 1936; Ringuette, 2007). Ellington and co-workers (Ellington et al., 1996) suggested that three mechanisms could potentially explain how spanwise flow could be generated. Our theoretical analysis, experimental test and literature survey show that 'centrifugal' acceleration in the boundary layer is the likely mechanism at the low *Re* of fruit flies. At high *Re*, the pressure gradient force can explain spanwise flow in the LEV core, whereas centrifugal pumping can explain spanwise flow behind the LEV. The region of spanwise flow is clearly not confined to the LEV core alone, at low and high Reynolds numbers, and its spatial distribution above an inclined wing depends strongly on Reynolds number (Birch et al., 2004; Aona et al., 2008). Our analysis further indicates that Coriolis acceleration is equally important in the stable attachment of the LEV, because this acceleration is an indispensable kinematic condition for the stable attachment of spanwise flow with respect to a revolving wing. All these experiments support, however, the hypothesis that spanwise flow balances the formation of vorticity at the leading edge and drains it into the tip vortex (Maxworthy, 1979; Ellington et al., 1996). The importance of *Ro*, and not *Re*, in determining LEV stability suggests further that vorticity transport in the large 'Ekman-like' separated flow region behind the LEV could be equally critical in maintaining this balance at low *Re*, compared with vorticity transport found in the LEV at high *Re*. We infer this from a prior study that suggests that the outward spiral flow within the core is *Re* dependent (Birch et al.,
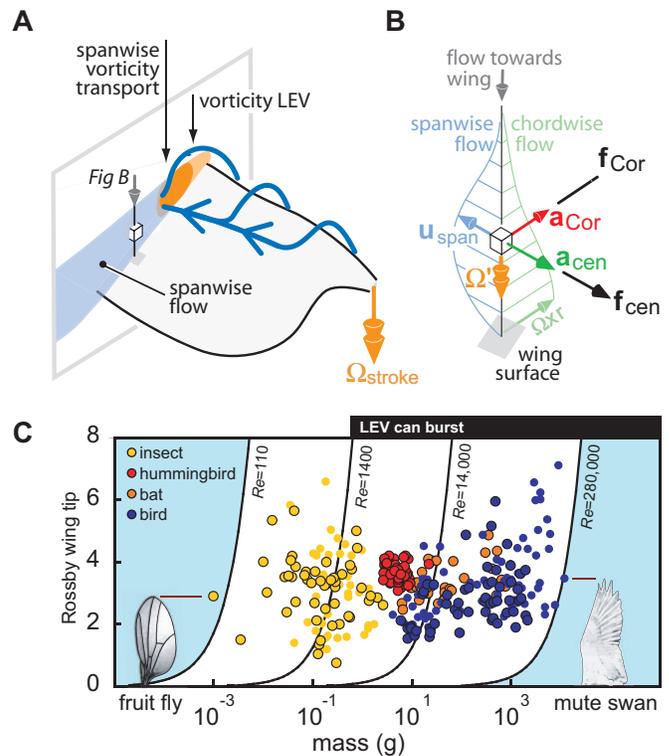

Fig. 12. Proposed 3D flow structure of a stable LEV and feasibility of its general use by flying animals. (A) Sketch of the local flow field on a revolving fruit fly wing at *Re*=110 and 1400 based on previously published particle image velocimetry (PIV) data (Birch et al., 2004) and Figs 1, 4 and 5. Spanwise flow is present in the whole region on top of the wing and convects the accumulating vorticity in the LEV towards the tip vortex. (B) The large spanwise flow region of the wing is mediated by the rotational accelerations a_{cen} and a_{Cor}, which results in an Ekman-like boundary layer, similar to that on spinning discs and wind turbine blades. The accelerations are balanced by the corresponding normalized centripetal (f_{cen}) and Coriolis (f_{Cor}) forces in the flow that can be composed out of pressure and friction forces. (C) Rossby number of animal wings assuming zero advance ratio as a function of body mass (*N*=319 in total). The average values are close to those found for fruit flies (*Ro*=2.9): insects *Ro*=3.1 (s.d.=1.1, *N*=98), hummingbirds *Ro*=3.7 (s.d.=0.3, *N*=65), bats *Ro*=3.3 (s.d.=0.4, *N*=39) and birds *Ro*=3.2 (s.d.=1.18, *N*=117). The circles with a black outline represent values that are directly based on the aspect ratio of one wing. Circles without a black outline represent values for which we corrected the aspect ratio of the tip-to-tip distance between paired wings and total wing surface such that we obtained the single-wing aspect ratio comparable to the calculation of the wingtip Rossby number. This amounted to subtracting the distance contributed by the body width between the wing bases. Information on this and all the insect, bird, hummingbird and bat wing morphology references can be found in Appendix 1. The constant–Reynolds number lines are calculated assuming an average C_L of 1.5 and represent the Reynolds numbers of our experiments and that of Himmelskamp (Himmelskamp, 1947); details are given in Appendix 2.

2004), whereas those results as well as our own suggest that LEV stability is not. Further, a direct analogy between LEVs on swept and revolving wings does not seem to hold for equally shaped wings operating at equally low Reynolds numbers, because we did not observe stable LEVs or force augmentation for swept fruit fly wings (Figs 1 and 2). In other experiments with high aspect ratio swept bird wings (*Apus apus*) a stable LEV was found (Videler et al., 2004; Lentink et al., 2007), but no significant force augmentation (lift coefficients lower than one) for

12,000<Re<77,000 (Lentink et al., 2007). This suggests that a direct analogy between LEVs on swept and revolving wings does not hold at higher Reynolds numbers either.

Link between Rossby number and 'quasi-steady' lift theory

This study supports an earlier notion that the aerodynamic force generation of insects might be considered 'quasi-steady', excluding the complications that occur during stroke reversal (Dickinson et al., 1999; Sane and Dickinson, 2001; Usherwood and Ellington, 2002). Quasi-steadiness implies that the instantaneous value of the flow velocity is more important than its instantaneous rate of change for understanding and predicting the aerodynamic forces, in particular wing lift (Sane and Dickinson, 2001). Our theoretical framework supports this idea, because the 'quasi-steady' rotational accelerations a_{cen} and a_{Cor} are responsible for LEV stability, whereas the unsteady angular acceleration a_{ang} is not. This is not to say that unsteadiness is not significant in insect flight. The translational reciprocating case resulted in an unstable LEV that still significantly augmented force, as found by Wang et al. (Wang et al., 2004), but this force is less than that found for revolving wings (Fig. 6). Further, LEV stability is less important for insects that employ considerably smaller stroke amplitude than fruit flies. For example, unloaded hovering bees use a narrow stroke amplitude (Φ_0=0.78 rad, compared with 1.2 rad for a fruit fly) resulting in a lower dimensionless stroke amplitude. Recent experiments indicate that bees depend more strongly on unsteady force augmentation at the start and end of the stroke (Altshuler et al., 2005), at which point angular acceleration is maximal and the rotational accelerations are minimal. This implies that unsteady lift mechanisms such as added mass effects and wake capture (Dickinson et al., 1999) become increasingly more significant, compared with 'quasi-steady' forces based on the stable LEV, when the dimensionless stroke amplitude decreases.

Lift augmentation at Reynolds numbers higher than 14,000

Our experiments (110<Re<14,000) and the experiments of others on a propeller (Re=280,000) and wind turbines (Re of order 10^6) suggest that lift augmentation is continuous in the inertial flow regime for Rossby numbers of order one. Ellington and Usherwood (Ellington and Usherwood, 2001) found, however, that revolving model hawkmoth wings operating at 10,000<Re<50,000 failed to produce high lift. The reason for this is unclear, and their findings for Re=10,000 contrast with ours at Re=14,000 and the high force coefficients found for quail wings at Re=26,000 by Usherwood and Ellington (Usherwood and Ellington, 2002). It could well be that airfoil shape plays a critical role in the apparent lift crisis for the thin and sharp model hawkmoth-like wings at 10,000<Re<50,000. Schmitz (Schmitz, 1942) found such a phenomenon for airfoils through wind tunnel experiments within this same range. He found that thin and sharp airfoils outperformed blunt and thick airfoils at low Re and *vice versa* at high Re. For these airfoils there exists a critical Re below which its lift decreases and its drag increases drastically. This is due to the presence of laminar separation bubbles and transitions to turbulent boundary layer flow that dominate airfoil performance at intermediate Re. This is relevant because the spinning wings tested by Ellington and Usherwood (Ellington and Usherwood, 2001) (at intermediate Re) featured thin and sharp, sub-critical, airfoils whereas the propeller (Himmelskamp, 1947) and wind turbine blades at high Re (Tangler, 2004) featured thick and blunt, super-critical airfoils. Ellington and Usherwood (Ellington and

Usherwood, 2001) tentatively conclude that the LEV is unstable on revolving wings at Re≥10,000 because of a lack of spanwise flow that stabilizes the LEV. The spanwise flow visualization of Himmelskamp (Himmelskamp, 1947) on a propeller at Re=280,000 (Fig. 11) and visualizations of stable LEVs on wind turbine blades (Beom-Seok et al., 2002), propeller fans (e.g. Simonich et al., 1992) and ship screws (e.g. Kerwin, 1986) operating at similar angles of attack and Ro, but at higher Re, contradict this idea. The work of Hubel and co-workers (Hubel, 2006) shows that a model goose flapping in the intermediate Reynolds number regime can, indeed, generate a stable LEV during forward flight. We conclude therefore that there is significant evidence that LEV-based force augmentation could exist continuously from revolving fruit fly wings to wind turbine blades at low Ro, but more research on the influence of airfoil shape on LEV generation, stability and force augmentation in the intermediate 10,000<Re<100,000 is needed.

Force augmentation of revolving wings in nature and technology

In summary, the single condition for LEV stability and maximal force augmentation appears to be a sufficiently low Ro. Thus, the use of LEVs to augment forces may be more widely distributed among swimming and flying animals than previously appreciated. In Fig. 12C, we show the results of a literature survey plotting Ro for hovering wings as a function of body mass. The distribution indicates that many large animals possess wings with a sufficiently low Ro to create stable LEVs (note that Ro at the all-important radius of gyration is roughly 50% lower than Ro calculated at the wing tip in Fig. 12C). This is not to suggest that all animals larger than insects can hover or create LEVs when flying at cruising speed, but that there is no aerodynamic reason why they could not make use of this mechanism during slow hovering flight or short take-off and landing when their advance ratio is small and Ro is of order one (e.g. see Fig. 11, spanwise flow decreases for higher advance ratios). LEVs, under low Ro conditions, have indeed been found on the wings of bats during hovering flight (Muijres et al., 2008). The elevated forces we measured at Re 14,000, a value appropriate for hummingbirds, is consistent with the putative observation of LEVs on hummingbird (Altshuler et al., 2004; Warrick et al., 2005) and quail (Usherwood and Ellington, 2002) wings. Finally, Hubel and co-workers found a stable LEV near the base of a flapping goose model in forward flight (Hubel, 2006). The local Rossby number is much lower near the wing base, like on wind turbine blades (see also Lentink and Dickinson, 2008), and can therefore locally support a stable LEV, even at relatively high advance ratios.

Because Reynolds number and stroke amplitude are not critical features in LEV stability, we think that a LEV could be an efficient high-lift mechanism for slow hovering animals, small and big. Our experiments suggest that aerodynamic efficiency is maximal for smaller LEVs generated at lower angles of attack, at increasingly higher Reynolds number (Figs 8 and 9). Total hovering efficiency, however, depends not only on aerodynamic efficiency but also on the efficiency of the muscles that drive the wing. During hovering, animal weight is balanced by vertical thrust, which is proportional to the product of lift coefficient, flapping frequency squared, and stroke amplitude squared. Noting that flapping frequency is confined to a narrow band for high muscle efficiency (McMahon, 1984), and that stroke amplitude is limited to 180° or less, a high maximum lift coefficient clearly helps to accommodate both the high vertical thrust needed to

balance weight during hovering and the much lower thrust needed during cruising.

Our theoretical frame work represents air and water equally well. The pectoral fins of many swimming animals flap similar to the wings of flying animals, not only for generating lift but also for generating drag to maneuver. Fig. 6 shows that revolving wings (unidirectional and reciprocating) not only generate more lift for their surface area but also generate much more drag at very high angles of attack, well beyond 45° For angles of attack above 45°, the attached leading and trailing edge vortex (LEV and TEV) on the model fly wings are surprisingly similar to the ones recently observed on the pectoral fin of a sun fish [Lauder and Madden in Bandyopadhyay et al. (Bandyopadhyay et al., 2008)]. The Rossby number based on the single-wing aspect ratio of fish pectoral fins is often low. For seven species described in the literature we found Ro=2.5 on average with s.d.=0.7 (references in Appendix 1), low enough values of Ro for stable LEVs. For completeness we also estimated an average Ro value of 3.7 for autorotating seeds (s.d.=1.14, N=26, references in Appendix 1). This suggests that a stable LEV could also explain the elevated lift forces found for these botanical structures (Azuma and Yasuda, 1989). We have recently tested this using 3D DPIV and will report the results elsewhere. With respect to technology, we envisage that micro air vehicles could more easily mimic nature and generate a stable LEV by simply adopting the only constraint for a stable LEV and force augmentation – revolving a wing continuously at low Rossby number, which is more efficient than flapping the same wing.

APPENDIX 1
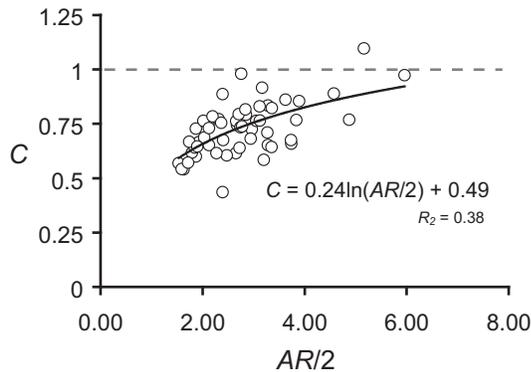**Rossby numbers of animal wings from insects to birds**

Fig. A1. Rossby numbers had only to be corrected for insects and birds. For insects we made use of photos of insects with extended wings, which resulted in an accurate correction (yellow circles without outline in Fig. 12C). For the corrected bird values (blue circles without outline in Fig. 12C) we could not obtain such accurate photos and proceeded as follows. First, we obtained a large data set of aspect ratios based on the full wing span (Tennekes, 1997). Subsequently, we compared these values with the ones for which we also obtained an accurate value of the single-wing aspect ratio (Slater Museum, 2005–2006, Online Wing collection of the Slater Museum of Natural History, University of Puget Sound, Tacoma, WA, USA; http://www.ups.edu/x5662.xml) and determined the required correction factor C based on the difference. We correlated the correction factor C to the aspect ratio of the full wing divided by two, AR/2. This factor was used to estimate the single-wing aspect ratio of the remaining bird wings with a conservative extrapolation r value for albatrosses (AR/2<7.5) that is close to one.

Table A1. Source of wing data

Insect wing data	Azuma, 2006
	Ellington, 1984
	Lehmann and Dickinson, 1998
	Marden, 1987
Hummingbird wing data	Altshuler, 2001
	Chai and Millard, 1997
	Stiles et al., 2005
Bat wing data	Hartman, 1963
	Jones et al., 2003
	Norberg et al., 2000
	Vaughan et al., 2004
Bird wing data	Slater Museum, 2005–2006*
	Tennekes, 1997
Fish pectoral fin data	Hove et al., 2001
	Combes and Daniel, 2001
	Walker and Westneat, 2002
	Walker, 2004
Autorotating seed wing data	Azuma and Yasuda, 1989
	Yamada and Suzuki, 1999

*Online Wing collection of the Slater Museum of Natural History, University of Puget Sound, http://www.ups.edu/x5662.xml.

APPENDIX 2
The relationship between *Ro*, mass and *Re*

The Reynolds and Rossby number (based on wing radius; single-wing span) in hovering flight are given by:

$$Re_g = \frac{\rho \overline{U_g} c}{\mu} \ (3.1) \tag{A1}$$

and

$$Ro = AR_s = \frac{b^2}{2S} = \frac{b}{2\overline{c}}, \tag{A2}$$

where Re_g is the Reynolds number at the radius of gyration. Note that b is the wing span, S the wing surface area and AR_s the single-wing aspect ratio. Force equilibrium in hovering flight requires that the following relation holds:

$$W = \overline{L} \rightarrow \overline{C_L} 1/2\rho\overline{U_g^2}S = mg, \tag{A3}$$

where W is the weight, $\overline{L}$ the time-averaged lift, $\overline{C_L}$ the time-averaged lift coefficient, m the mass and g the gravitational constant. We now approximate the time-averaged velocity with the r.m.s. time-averaged velocity which results in:

$$\overline{U_g} \approx \sqrt{\overline{U_g^2}} = \sqrt{\frac{mg}{\overline{C_L} 1/2\rho S}}. \tag{A4}$$

Combining Eqns A1, A2 and A4, we obtain the Reynolds number as a function of the total mass and the wingtip Rossby number for hovering flight:

$$Re_g = \frac{\rho\overline{U_g}c}{\mu} \approx \sqrt{\frac{mg}{\overline{C_L}} \times \frac{\rho}{\mu^2} \times \frac{2c^2}{S}} = \sqrt{\frac{mg}{\overline{C_L}} \times \frac{\rho}{\mu^2} \times \frac{1}{Ro}}. \tag{A5}$$

We plotted Reynolds number isolines of hovering animal wings in Fig. 12C by assuming a time-averaged lift coefficient of 1.5 for the full weight range from insects to birds. In doing so, we assume the animal is making use of a LEV and operates at a high lift coefficient of C_L=1.5. This approximation suffices for the Reynolds number of which the exact value is less relevant.

LIST OF ABBREVIATIONS

α	wing angle of attack
α_0	wing angle of attack amplitude
Φ_0	wing stroke amplitude (half the total stroke amplitude Φ)
ν	kinematic viscosity
ρ	fluid density
$\boldsymbol{\Omega}$	angular velocity of the rotating frame
$\boldsymbol{\Omega}_{stroke}$	angular velocity due to wing stroke
$\dot{\boldsymbol{\Omega}}$	angular acceleration of the rotating frame
$\dot{\boldsymbol{\Omega}}_{stroke}$	angular acceleration due to wing stroke
$\boldsymbol{\Omega}'$	angular velocity of the fluid separated from the fly wing
$\mathbf{a}_{ang}$	angular acceleration
$\mathbf{a}_{cen}$	centripetal acceleration
$\mathbf{a}_{Cor}$	Coriolis acceleration
$\mathbf{a}_{inert}$	acceleration with respect to inertial coordinate system
$\mathbf{a}_{loc}$	acceleration with respect to local coordinate system
A^*	stroke amplitude
AR	tip to tip wing aspect ratio
AR_s	single-wing aspect ratio
b	burst vortex (Fig. 4)
b_s	single-wing span
c	average wing chord length
C	correction factor wing aspect ratio data
C_L	lift coefficient
C_D	drag coefficient
C_{D0}	drag coefficient at zero lift
CFD	computational fluid dynamic
$\mathbf{D}$	drag force
$\mathbf{D}_{chord}$	chordwise drag force
DPIV	digital particle image velocimetry
Ek	Ekman number
$\mathbf{f}_{cen}$	specific centripetal force (per unit of volume)
$\mathbf{f}_{Cor}$	specific Coriolis force (per unit of volume)
g	gravitational constant
J	advance ratio
$\overline{L}$	time-averaged lift
$\mathbf{L}$	lift force
LEV	leading edge vortex
m	mass
N	number of experiments
r	magnitude of radius vector
$\mathbf{r}$	position of a fluid particle in the rotating frame
R	wing radius
R_g	wing radius of gyration
Re	Reynolds number
Re_g	Reynolds number at the radius of gyration
Ro	Rossby number
r.m.s.	root mean square
s	distance traveled in chord lengths
S	single-wing area
sb	spiral burst vortex (Fig. 4)
s.d.	standard deviation
s_g	number of chord lengths traveled at R_g during a full stroke (Fig. 3)
U_g	average velocity at the radius of gyration
$\mathbf{u}_{loc}$	velocity in local coordinate system
V	velocity along wing radius
W	weight
(x, y, z)	local coordinate system

REFERENCES

Altshuler, D., Dudley, R. and Ellington, C. P. (2004). Aerodynamic forces of revolving hummingbird wings and wing models. *J. Zool. Lond.* **264**, 327-332.

Altshuler, D. L. (2001). Ecophysiology of hummingbird flight along elevational gradients: an integrated approach. PhD Thesis, Univerisity of Texas at Austin, USA.

Altshuler, D. L., Dickson, W. B., Vance, J. T., Roberts, S. P. and Dickinson, M. H. (2005). Short-amplitude high-frequency wing strokes determine the aerodynamics of honeybee flight. *Proc. Natl. Acad. Sci. USA* **102**, 18213-18218.

Aono, H., Liang, F. and Liu, H. (2008). Near- and far-field aerodynamics in insect hovering flight: an integrated computational study. *J. Exp. Biol.* **211**, 239-257.

Azuma, A. (2006). *The Biokinetics of Flying and Swimming.* Reston, VA: AIAA Books.

Azuma, A. and Yasuda, K. (1989). Flight performance of rotary seeds. *J. Theor. Biol.* **138**, 23-53.

Bandyopadhyay, P. R., Beal, D. N. and Menozzi, A. (2008). Biorobotic insights into how animals swim. *J. Exp. Biol.* **211**, 206-214.

Baruh, H. (1999). *Analytical Dynamics.* New York: McGraw-Hill.

Beom-Seok, K., Jeong-Hwan, K., Koji, K., van Rooij, R. P. and Young-Ho, L. (2002). 3D Numerical predictions of horizontal axis wind turbine power characteristics of the scaled Delft university T40/50 model. Nagoya, Japan: Fifth JSME-KSME Fluids Engineering Conference.

Birch, J. M., Dickinson, M. H. (2001). Spanwise flow and the attachment of the leading-edge vortex on insect wings. *Nature* **412**, 729-733.

Birch, J. M., Dickinson, M. H. (2003). The influence of wing-wake interactions on the production of aerodynamic forces in flapping flight. *J. Exp. Biol.* **206**, 2257-2272.

Birch, J. M., Dickson, W. B. and Dickinson, M. H. (2004). Force production and flow structure of the leading edge vortex on flapping wings at high and low reynolds numbers *J. Exp. Biol.* **207**, 1063-1072.

Chai, P. and Millard, D. (1997). Flight and size constraints: hovering performance of large hummingbirds under maximal loading. *J. Exp. Biol.* **200,** 2757-2763.

Combes, S. A. and Daniel, T. L. (2001). Shape, flapping and flexion: wing and fin design for forward flight. *J. Exp. Biol.* **204**, 2073-2085.

Dickinson, M. H. (1994). The effects of wing rotation on unsteady aerodynamic performance at low Reynolds numbers. *J. Exp. Biol.* **192**, 179-206.

Dickinson, M. H. and Götz, K. G. (1993). Unsteady aerodynamic performance of model wings at low Reynolds numbers. *J. Exp. Biol.* **174**, 45-64.

Dickinson, M. H., Lehmann, F. O. and Sane, S. P. (1999). Wing rotation and the aerodynamic basis of insect flight. *Science* **284**, 1954-1960.

Dickson, W. B. and Dickinson, M. H. (2004). The effect of advance ratio on the aerodynamics of revolving wings. *J. Exp. Biol.* **207**, 4269-4281.

Dumitrescu, H. and Cardos, V. (2003). Rotational effects on the boundary-layer flow in wind turbines. *AIAA J.* **42**, 408-411.

Ellington, C. P. (1984). The aerodynamics of insect flight I-VI. *Philos. Trans. R. Soc. Lond. B Biol. Sci.* **305**, 1-181.

Ellington, C. P. and Usherwood, J. R. (2001). Lift and drag characteristics of rotary and flapping wings. In *Fixed and Flapping Wing Aerodynamics for Micro Air Vehicle Applications.* (ed. T. J. Mueller). Reston, VA: AIAA books.

Ellington, C. P., Van den Berg, C., Willmott, A. P. and Thomas, A. L. R. (1996). Leading-edge vortices in insect flight. *Nature* **384**, 626-630.

Fry, S. N., Sayaman, R. and Dickinson, M. H. (2003). The aerodynamics of free-flight maneuvers in Drosophila. *Science* **300**, 495-498.

Greenwell, D. I. (2002). Simple engineering model for delta-wing vortex breakdown. *J. Aircraft* **40**, 402-405.

Greitzer, E. M., Tan, C. S. and Graf, M. B. (2004). *Internal Flow Concepts and Applications.* Cambridge: Cambridge University Press.

Hartman, F. A. (1963). Some flight mechanics of bats. *Ohio J. Sci.* **53**, 59-65.

Himmelskamp, H. (1947). Profile investigations on a rotating airscrew. Dissertation Göttingen 1945, Reports and Translations No. 832.

Hove, J. R., O'Bryan, L. M., Gordon, M. S., Webb, P. W. and Weihs, D. (2001). Boxfishes (Teleostei: Ostraciidae) as a model system for fishes swimming with many fins: kinematics. *J. Exp. Biol.* **204**, 1459-1471.

Hubel, T. (2006). Untersuchungen zur instationären Aerodynamik an einem vogelähnlichen Flügelschlagmodell, PhD thesis, TU Darmstadt, Fachbereich Biologie.

Jones, G., Webb, P. I., Sedgeley, J. A. and O'Donnell, C. F. J. (2003). Mysterious Mystacina: how the New Zealand short-tailed bat (*Mystacina tuberculata*) locates insect prey. *J. Exp. Biol.* **206**, 4209-4216.

Kerwin, J. E. (1986). Marine propellers. *Annu. Rev. Fluid Mech.* **18**, 367-403.

Lehmann, F. O. and Dickinson, M. H. (1998). The control of wing kinematics and flight forces in fruit flies (*Drosophila spp.*). *J. Exp. Biol.* **201**, 385-401.

Lentink, D. and Dickinson, M. H. (2009). Biofluiddynamic scaling of flapping, spinning and translating fins and wings. *J. Exp. Biol.* **212**, 2691-2704.

Lentink, D., Müller, U. K., Stamhuis, E. J., de Kat, R., van Gestel, W., Veldhuis, L. L. M., Henningsson, P., Hedenström, A., Videler, J. J. and van Leeuwen, J. L. (2007). How swifts control their glide performance with morphing wings. *Nature* **446**, 1082-1085.

Lentink, D., Muijres, F. T., Donker-Duyvis, F. J. and van Leeuwen, J. L. (2008). Vortex-wake interactions of a flapping foil that models animal swimming and flight. *J. Exp. Biol.* **211**, 267-273.

Lindenburg, C. (2004). *Modelling of Rotational Augmentation Based on Engineering Considerations and Measurements.* London: European Wind Energy Conference.

Lu, Y., Shen, G. X. and Lai, G. J. (2006). Dual leading-edge vortices on flapping wings. *J. Exp. Biol.* **209**, 5005-5016.

Marden, H. J. (1987). Maximum lift production during takeoff in flying animals. *J. Exp. Biol.* **130**, 235-258.

Maxworthy, T. (1979). Experiments on the Weis-Fogh mechanism of lift generation by insects in hovering flight. Part 1. Dynamics of the 'fling'. *J. Fluid Mech.* **93**, 47-63.

McMahon, T. A. (1984). *Muscles, Reflexes and Locomotion.* Princeton, NJ: Princeton University Press.

Miller, L. A. and Peskin, C. S. (2004). When vortices stick: an aerodynamic transition in tiny insect flight. *J. Exp. Biol.* **207**, 3073-3088.

Muijres, F. T., Johansson, L. C., Barfield, R., Wolf, M., Spedding, G. R. and Hedenström, A. (2008). Leading-edge vortex improves lift in slow-flying bats. *Science* **319**, 1250-1253.

Norberg, U. M., Brooke, A. P. and Trewhella, W. J. (2000). Soaring and non-soaring bats of the family *pteropodidae* (flying foxes, *Pteropus* spp.): wing morphology and flight performance. *J. Exp. Biol.* **203**, 651-664.

Poelma, C., Dickson, W. B. and Dickinson, M. H. (2006). Time-resolved reconstruction of the full velocity field around a dynamically-scaled flapping wing. *Exp. Fluids* **41**, 213-225.

Ringuette, M., Milano, M. and Gharib, M. (2007). Role of the tip vortex in the force generation of low-aspect-ratio normal flat plates. *J. Fluid Mech.* **581**, 453-468.

Rossby, C. G. (1936). On the momentum transfer at the sea surface. Part I Papers *Phys. Oceanogr. Meteorol.* 3 no 3.

Ruijgrok, G. J. J. (1994). *Elements of Airplane Performance.* Delft, The Netherlands: Delft University Press.

Sane, S. P. and Dickinson, M. H. (2001). The control of flight force by a flapping wing: lift and drag production. *J. Exp. Biol.* **204**, 2607-2626.

Schlichting, H. (1979). *Boundary-Layer Theory*, 7th edn. New York: McGraw-Hill.

Schmitz, F. W. (1942). Aerodynamik des flugmodells, C.J.E. Volckmann Nachf. E. Wette, Berlin.

Simonich, J., McCormick, D. and Haas, R. (1992). Flow visualization of a prop-fan leading edge vortex at takeoff. *AIAA* **0386**.

Srygley, R. B. and Thomas, A. L. R. (2002). Unconventional lift-generating mechanisms in free-flying butterflies. *Nature* **420**, 660-664.

Stepniewski, W. Z. and Keys, C. N. (1984). *Rotary-Wing Aerodynamics.* Mineola, NY: Dover Publications.

Stiles, F. G., Altshuler, D. L. and Dudley, R. (2005). Wing morphology and flight behaviour of some North American hummingbird species. *Auk* **122**, 872-886.

Sun, M. and WU, J. (2004). Large aerodynamic forces on a sweeping wing at low Reynolds number. *Acta Mechanica Sinica* **20**, 24-31.

Tangler, J. L. (2004). Insight into wind turbine stall and post-stall aerodynamics. *Wind Energy* **7**, 247-260.

Tennekes H. (1997). *The Simple Science of Flight.* Cambridge, MA: The MIT Press.

Usherwood, J. R. and Ellington, C. P. (2002). The aerodynamics of revolving wings I-II. *J. Exp. Biol.* **205**, 1547-1576.

Van Den Berg, C. and Ellington, C. P. (1997). The three-dimensional leading-edge vortex of a 'hovering' model hawkmoth. *Philos. Trans. R. Soc. Lond. B Biol. Sci.* **352**, 329-340.

Vanyo, J. P. (1993). *Rotating Fluids in Engineering and Science.* Mineola, NY: Dover Publications.

Vaughan, N., Parsons, S., Barlow, K. E. and Gannon, M. R. (2004). Echolocation calls and wing morphology of bats from the west indies. *Acta Chiropter.* **6**, 75-90.

Videler, J. J., Stamhuis, E. J. and Povel, G. D. E. (2004). Leading-edge vortex lifts swifts. *Science* **306**, 1960-1962.

Walker, J. A. (2004). Dynamics of pectoral fin rowing in a fish with an extreme rowing stroke: the threespine stickleback (*Gasterosteus aculeatus*) *J. Exp. Biol.* **207**, 1925-1939.

Walker, J. A. and Westneat, M. W. (2002). Performance limits of labriform propulsion and correlates with fin shape and motion. *J. Exp. Biol.* **205**, 177-187.

Wang, Z. J. (2008). Aerodynamic efficiency of flapping flight: analysis of a two-stroke model *J. Exp. Biol.* **211**, 234-238.

Wang, Z. J., Birch, J. M. and Dickinson, M. H. (2004). Unsteady forces and flows in low Reynolds number hovering flight: two-dimensional computations vs robotic wing experiments *J. Exp. Biol.* **207**, 449-460.

Warrick, D. R., Tobalske, B. W. and Powers, D. R. (2005). Aerodynamics of the hovering hummingbird. *Nature* **435**, 1094-1097.

Winter, H. (1936). Flow phenomena on plates and airfoils of short span. NACA Report 798.

Yamada, T. and Suzuki, E. (1999). Comparative morphology and allometry of winged diaspores among the Asian Sterculiaceae. *J. Trop. Ecol.* **15**, 619-635.